FRONTIERS OF PHYSICS

RESEARCH ARTICLE
Volume 19 / Issue 6 / 63207 / 2024

First-principles investigation of two-dimensional iron molybdenum nitride: A double transition-metal cousin of $MoSi_2N_4$(MoN) monolayer with distinctive electronic and topological properties

Yi Ding[1,†], Yanli Wang[2,‡]

1 School of Physics, Hangzhou Normal University, Hangzhou 311121, China
2 Department of Physics, Zhejiang Sci-Tech University, Hangzhou 310018, China
E-mail: †dingyi2001@tsinghua.org.cn, ‡wangyanli-04@tsinghua.org.cn
Received April 21, 2024; accepted June 11, 2024

© Higher Education Press 2024

ABSTRACT

As the homologous compounds of $MoSi_2N_4$, the $MoSi_2N_4(MoN)_n$ monolayers have been synthesized in a recent experiment. These systems consist of homogeneous metal nitride multilayers sandwiched between two SiN surfaces, which extends the septuple-atomic-layer MSi_2N_4 system to ultra-thick $MSi_2N_4(MN)_n$ forms. In this paper, we perform a first-principles study on the $MoSi_2N_4$(FeN) monolayer, which is constructed by iron molybdenum nitride intercalated into the SiN layers. As a cousin of $MoSi_2N_4$(MoN), this double transition-metal system exhibits robust structural stability from the energetic, mechanical, dynamical and thermal perspectives. Different from the $MoSi_2N_4$(MoN) one, the $MoSi_2N_4$(FeN) monolayer possesses intrinsic ferromagnetism and presents a bipolar magnetic semiconducting behaviour. The ferromagnetism can be further enhanced by the surface hydrogenation, which raises the Curie temperature to 310 K around room temperature. More interestingly, the hydrogenated $MoSi_2N_4$(FeN) monolayer exhibits a quantum anomalous Hall (QAH) insulating behaviour with a sizeable nontrivial band gap of 0.23 eV. The nontrivial topological character can be well described by a two-band $\boldsymbol{k}\cdot\boldsymbol{p}$ model, confirming a non-zero Chern number of $C=1$. Similar bipolar magnetic semiconducting feature and hydrogenation-induced QAH state are also present in the WSi_2N_4(FeN) monolayer. Our study demonstrates that the double transition-metal MSi_2N_4(M′N) system will be a fertile platform to achieve fascinating spintronic and topological properties.

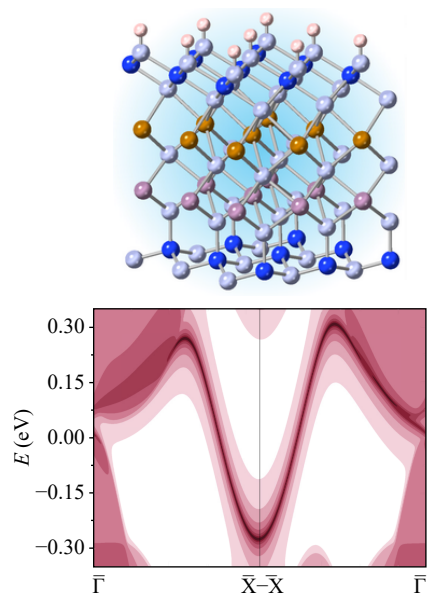

Keywords quantum anomalous Hall state, MA_2Z_4(M′Z) family, first-principles, double transition-metal nitride

1 Introduction

Since the experimental synthesis of two-dimensional (2D) $MoSi_2N_4$ material [1], the septuple-atomic-layer MA_2Z_4 monolayers, where M is the transition-metal, A is Si or Ge, and Z is the nitrogen group element, have attracted sufficient scientific attention due to their unique geometric structures and extraordinary electronic properties [2, 3]. Taking $MoSi_2N_4$ as an example, it has been fabricated by introducing elemental silicon during the chemical vapor deposition growth of molybdenum nitride [1, 4]. The surfaces of molybdenum nitride layer

Higher Education Press
https://doi.org/10.1007/s11467-024-1431-6

are passivated by the SiN hexagonal layers, forming a septuple-atomic-layer geometry with the stacking sequence of N–Si–N–Mo–N–Si–N [5]. This $MoSi_2N_4$ monolayer can be viewed as a MoS_2-like MoN_2 sheet sandwiched between two SiN layers. Similar to the MoS_2 system, the $MoSi_2N_4$ monolayer exhibits a semiconducting behaviour with a moderate band gap [6]. Intriguing valley-dependent properties, including the spin-valley coupling, valley-contrasting Berry curvature, and valley-selective optical circular dichroism, are present in this $MoSi_2N_4$ system [7, 8]. Besides that, many other exceptional properties also emerge in the $MoSi_2N_4$ and related group-VI MA_2Z_4 systems, such as the protected band edge states [9], high lattice thermal conductivity [10], large piezoelectric coefficients [11], and anisotropic carrier mobilities [12], which render them promising materials for nanoelectrics, valleytronics and spintronics applications.

For the MA_2Z_4 family materials, the metal composition plays a crucial role in their electronic properties [13]. It has been found that there is an odd–even rule in the $4d$ and $5d$ MSi_2N_4 systems, for which the group-IV/VI metals with an even number of valence electrons give rise to a semiconducting behaviour while the group-III/V metals with an odd number of valence electrons lead to a metallic feature [14, 15]. In particular, for the case of M = Y and Nb, a spontaneous spin-polarization emerges in the MSi_2N_4 monolayers [14]. The spin-polarization also appears in the $3d$ MSi_2N_4 systems with M = V, Cr, Mn, Fe, and Co, which can be further tuned to half-metals by carrier dopings [16, 17]. Especially, the VSi_2N_4 monolayer is a ferromagnetic semiconductor with valley-constrasting physical properties, which can be converted to a QAH insulator through the modulation of external strain, electric field or correlation effects [18, 19]. In addition to the VSi_2N_4 system, several V-based derivatives, such as the $VN_2X_2Y_2$ (X = group-III and Y = group-VI elements)[20], $VSiXN_4$ (X = C, Si, Ge, Sn, Pb) [21–23], and Janus $SVAN_2$ (A = Si, Ge) [24] monolayers, have been proposed with tunable electronic and topological properties.

It would be noted that novel topological states, such as the QAH insulating state, are mainly distributed in the group-V MA_2Z_4 systems [18–23, 25]. Those QAH insulators represent a novel quantum state that possesses a finite Chern number and chiral edge states within the insulating bulk [26]. The edge states are topologically protected and robust against scattering, making QAH systems promising candidates for applications in low-power electronic devices. Several 2D systems, such as the XY (X = K, Rb, Cs; Y = N, P, As, Sb, Bi) [27], FeX_3 (X = Cl, Br, I) [28], V_2O_3 [29], and SiC-supported silicene [30], have been proposed as potential QAH insulators. In the experiments, the intriguing QAH effect has already been observed in the V-doped $(Bi, Sb)_2Te_3$, $MnBi_2Te_4$, and moiré graphene systems [26]. However for the experimentally synthesized group-VI MSi_2N_4 ones, such nontrivial topological feature has not been reported in the literature yet [2]. Even for a distorted T′-phase geometry with Mo zigzag chains, the T′-$MoSi_2N_4$ monolayer is still a trivial metal [31], not a quantum spin Hall insulator like the T′-MoS_2, T′-$MoSi_2P_4$ and T′-$MoGe_2P_4$ systems [32, 33]. Although the QAH insulating state can be induced in the graphene, MoS_2 and transition-metal dichalcogenides (TMDs) by incorporation of transition metals [34, 35], the substitution or decoration of transition metal atoms in the $MoSi_2N_4$ monolayer can not trigger a nontrivial topological behavior [36, 37].

Very recently, a series of $MoSi_2N_4(MoN)_n$ systems have been fabricated in the experiment [38]. These ultra-thick $MoSi_2N_4(MoN)_n$ monolayers are homologous compounds of $MoSi_2N_4$, which contain the MoN multilayers that are intercalated between two SiN surface layers. Different from the semiconducting $MoSi_2N_4$ system [38], all the $MoSi_2N_4(MoN)_n$ monolayers are metals and the metallicity originates from the inner MoN multilayers. The synthesis of $MoSi_2N_4(MoN)_n$ extends the septuple-atomic-layer MSi_2N_4 system to the ultra-thick $MSi_2N_4(MN)_n$ form. There are multiple MN layers in the $MSi_2N_4(MN)_n$ materials, which would accommodate heterogeneous metal nitride layers beyond the MoN ones. In a recent work, a double transition-metal $W_2TiSi_2N_6$ system is proposed, which is composed of metal nitride multilayers with a sequence of N–W–N–Ti–N–W–N between the SiN surface layers [39]. Owing to the hybridization of W and Ti d orbitals, a quantum spin Hall insulating state appears in this double transition-metal system. It is worth mentioning that the bulk materials of double transition-metal nitrides $M'MN_2$ (M′ = Cr, Mn, Fe, Co, Ni; M = Ta, Mo, W) have already been synthesized in the experiment [40]. Besides, thin films of $FeMoN_2$ and $FeWN_2$ have also been fabricated by the polymer-assisted deposition [41]. Inspired by these progresses, we perform a theoretical study on the group-VI $MSi_2N_4(FeN)$ monolayers, for which the central part just contains one $FeMN_2$ unit (M = Mo, W). We find that owing to the existence of Fe layer, the $MSi_2N_4(FeN)$ monolayers possess intrinsic ferromagnetism with a bipolar magnetic semiconducting feature. The ferromagnetism can be enhanced by the surface hydrogenation, which further converts the $MSi_2N_4(FeN)$ system into a promising quantum anomalous Hall insulator.

2 Methods

First-principles calculations are performed by the VASP code [42], which adopts Perdew–Burke–Ernzerhof (PBE) projector augmented wave pseudopotentials and plane-wave basis sets with an energy cut-off of 520 eV. A vacuum layer of more than 15 Å is used to simulate the

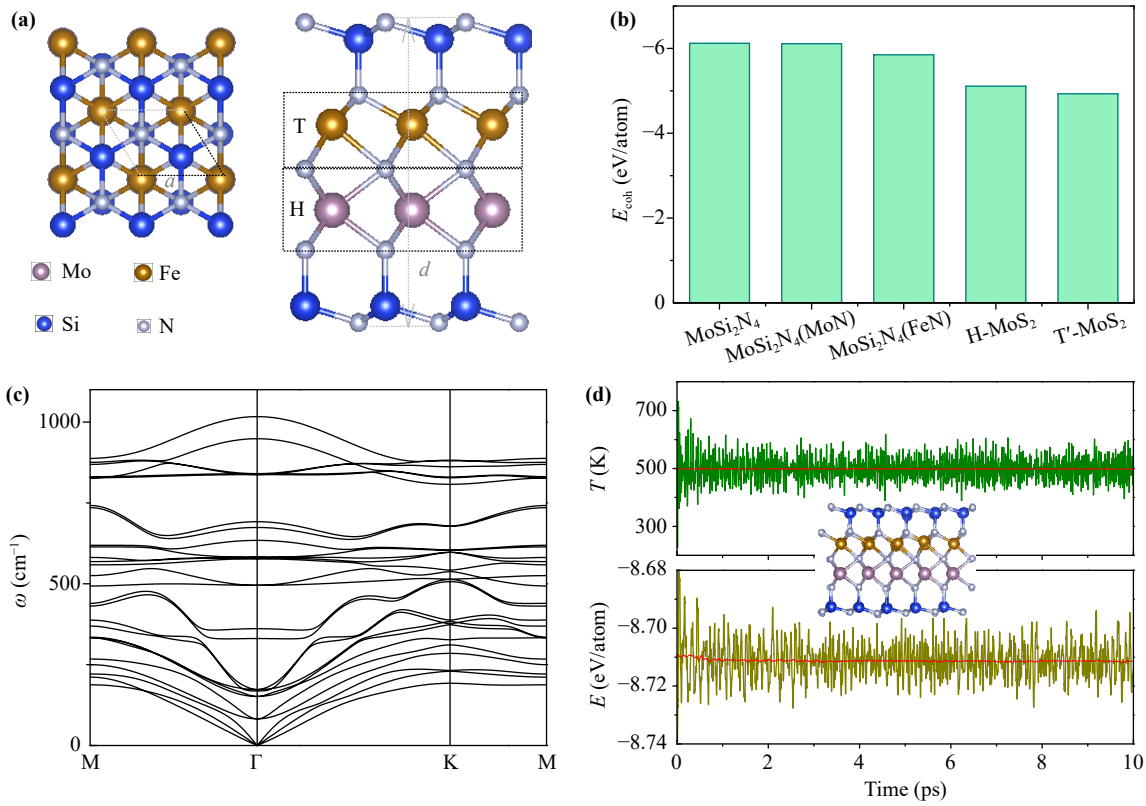

Fig. 1 **(a)** The top and lateral view of the geometrical structure of $MoSi_2N_4$(FeN) monolayer. The in-plane lattice constant (a) and thickness (d) of system are marked. The dashed rectangles denote the overlapping FeN_2 and MoN_2 layers, where the letters T and H represent the octahedral and trigonal prismatic coordinations of metal atoms, respectively. **(b)** A comparison of cohesive energies of the $MoSi_2N_4$(FeN) monolayer and experimentally synthesized Mo-based 2D materials. **(c)** The phonon dispersions and **(d)** AIMD simulation results of $MoSi_2N_4$(FeN) monolayer. For clarity, the average values of adjacent data in 1 ps are depicted as dotted lines in (d). The final configuration after the AIMD simulation is also displayed.

isolated 2D system. The Γ-centered $18 \times 18 \times 1$ and $24 \times 24 \times 1$ **k**-meshes are utilized for the relaxation and static calculations, respectively. Geometries are fully optimized until the maximum residual force is less than 0.005 eV/Å on each atom. Despite of the PBE functional, we also check whether a Hubbard U is needed to apply on the Fe atoms. Using the $FeMoN_2$ bulk as a reference, we find that with a common effective U value of 3–4 eV on the Fe 3d orbitals [43], the PBE+U calculation shows the $FeMoN_2$ bulk is an indirect semiconductor, which is in sharp contrast to the metallic behaviour from the experimental observation [44]. When a small U value of 1–2 eV is utilized, the PBE+U results are very similar to the PBE ones. Since the PBE calculation can predict reasonable result on the $FeMoN_2$ bulk, the Hubbard U is not employed in the present work. Instead, a hybrid functional of Heyd–Scuseria–Ernzerhof (HSE) is further used to examine the semiconducting behavior, which adopts the HSE06 form with a screening parameter of 0.2 $Å^{-1}$. The dynamic stability of systems is examined by the Phonopy code [45], and the thermal stability is checked by the *ab initio* molecular dynamic (AIMD) simulations, which are performed on a canonical (NVT) ensemble with a Nosé thermostat at 500 K. The step time is set to 1 fs and the total simulated time is 10 ps, i.e., 10^4 steps.

3 Results and discussion

3.1 Structure and stability of $MoSi_2N_4$(FeN) monolayer

The geometrical structure of $MoSi_2N_4$(FeN) monolayer is depicted in Fig. 1(a), which is composed of nine atomic layers with a stacking sequence of N–Si–N–Mo–N–Fe–N–Si–N. It is a heterogeneous cousin of $MoSi_2N_4$(MoN) monolayer and can be viewed as the overlapping MoN_2 and FeN_2 layers sandwiched between two buckled SiN honeycombs. The Mo atoms form a trigonal prismatic (H) geometry with the six neighboring N atoms, while the Fe atoms have an octahedral (T) geometry instead. Such H_{Mo}–T_{Fe} stacking structure is energetically more stable than the H_{Mo}–H_{Fe}, T_{Mo}–H_{Fe}, and T_{Mo}–T_{Fe} ones by 0.77, 1.43, and 0.74 eV per formula unit (f.u.), respectively. The favorable geometry of $MoSi_2N_4$(FeN) monolayer is consistent with the

$FeMoN_2$ bulk, where alternated Mo and Fe layers adopt the trigonal prismatic and octahedral geometries, respectively [44]. The electron localization function (ELF) of $MoSi_2N_4$(FeN) monolayer is further provided in Fig. S1 of the Electronic Supplementary Materials (ESM). It can be seen that for the Fe–N and Mo–N bonds, electrons are mainly localized around the N atoms, indicating these bonds exhibit an ionic bonding character. On the other hand, the Si–N bonds present a covalent nature, for which the electrons are localized in the middle region between Si and N atoms. The in-plane lattice constant (a) of the $MoSi_2N_4$(FeN) monolayer is 2.89 Å, which is similar to those of the $FeMoN_2$ bulk (2.84 Å) [44] and $MoSi_2N_4$(MoN) monolayer (2.91 Å) [38]. The thickness between the top and bottom N atomic layers is 9.39 Å, a little smaller than the $MoSi_2N_4$(MoN) one (9.77 Å) [38]. This is mainly attributed to the smaller thicknesses of FeN_2 layer (2.32 Å) in the $MoSi_2N_4$(FeN) monolayer than that of the MoN_2 layer (2.63 Å) in the $MoSi_2N_4$(MoN) counterpart. When the spin–orbit coupling (SOC) effect is included in the structural relaxation, the obtained lattice constant and thickness are 2.89 and 9.40 Å, which are similar to the PBE results. The PBE+U calculations with different U values of 1–4 eV are further performed on the $MoSi_2N_4$(FeN) monolayer. As shown in Fig. S2 of the ESM, the in-plane lattice constant a is insensitive to the U value, which is always around 2.90 Å. On the other hand, the thickness of FeN_2 layer is varied with the increase of U, and the charge transfer between Fe and N atoms is also changed evidently under different U values. Consequentially, the electrostatic potential difference in the $MoSi_2N_4$(FeN) monolayer exhibit a noticeable U-dependent behavior. In the literature, the common used U value for the Fe d orbitals is 3–4 eV [43], but we find it is inappropriate for the layered iron molybdenum nitride as stated in the method section. For small U values less than 2 eV, the PBE+U results resemble the PBE ones. Thus the Hubbard U is ignored for the $MoSi_2N_4$(FeN) monolayer.

The cohesive energy ($E_{\rm coh}$), defined as the difference between the total energy of compound and the sum of energies of composed atoms, is calculated for the $MoSi_2N_4$(FeN) monolayer as shown in Fig. 1(b). Following this definition, a more negative $E_{\rm coh}$ value corresponds to a more energetically stable structure. The obtained $E_{\rm coh}$ of $MoSi_2N_4$(FeN) monolayer is –5.85 eV/atom, which is comparable to the data of $MoSi_2N_4$(MoN) (–6.11 eV/atom) and $MoSi_2N_4$ monolayers (–6.12 eV/atom), and is evidently more negative than those of the H-MoS_2 (–5.11 eV/atom) and T'-MoS_2 (–4.93 eV/atom) monolayers. It indicates the $MoSi_2N_4$(FeN) monolayer will have a good energetic stability akin to these experimentally synthesized Mo-based 2D materials. We further calculate the formation energy ($E_{\rm form}$) of $MoSi_2N_4$(FeN) monolayer, which is defined as $E_{\rm form} = (E_{\rm MoSi_2N_4(FeN)} - E_{\rm Mo-bulk} - E_{\rm Fe-bulk} - 2E_{\rm Si-bulk} - \frac{5}{2}E_{\rm N2-gas})/9$. Here, the $E_{\rm MoSi_2N_4(FeN)}$ is the total energy of $MoSi_2N_4$(FeN) monolayer, $E_{\rm Mo-bulk}$, $E_{\rm Fe-bulk}$ and $E_{\rm Si-bulk}$ are the energies of Mo, Fe and Si atoms in their stable bulk forms, and $E_{\rm N2-gas}$ denotes the energy of an isolated N_2 molecule. The corresponding $E_{\rm form}$ is calculated to –0.69 eV/atom for the $MoSi_2N_4$(FeN) monolayer. Such negative $E_{\rm form}$ value indicates the formation of $MoSi_2N_4$(FeN) monolayer will be an exothermic process from the elemental compounds of its components, which is advantageous for the experimental synthesis. The phonon dispersions of $MoSi_2N_4$(FeN) monolayer are calculated to verify its dynamical stability in Fig. 1(c). It can be seen that there are no soft modes and all the frequencies in the Brillion zone are positive, demonstrating the robust dynamical stability of $MoSi_2N_4$(FeN) monolayer. The AIMD simulation is further performed on the $MoSi_2N_4$(FeN) monolayer as shown in Fig. 1(d). The temperature and total energy just fluctuate around the equilibrium value without sudden changes during the 10 ps simulation. The structural integrity of system is well preserved after the AIMD simulation and there is no bond breaking in the final structure. This confirms the good thermal stability of $MoSi_2N_4$(FeN) monolayer at a temperature of 500 K.

Besides that, utilizing the energy-vs-strain method, the elastic constants of $MoSi_2N_4$(FeN) monolayer are obtained as $C_{11} = 615$ and $C_{12} = 189$ N/m, respectively. These values satisfy the Born–Huang criteria for a 2D hexagonal lattice ($C_{11} > C_{12} > 0$) [46], confirming the mechanical stability of $MoSi_2N_4$(FeN) monolayer. The corresponding Young's modulus (Y) is evaluated as $Y = (C_{11}^2 - C_{12}^2)/[C_{11} \times (d + 2r_N)]$ [38], where d is the thickness of system and r_N is the van der Waals radius of surface N atom. For the $MoSi_2N_4$(FeN) monolayer, the Young's modulus Y is calculated as 446 GPa, which is comparable to those of $MoSi_2N_4$(MoN) and $MoSi_2N_4$ systems (490 and 491.4±139.1 GPa) [1, 38]. Its Poisson ratio (ν) is evaluated as $\nu = C_{12}/C_{11} = 0.31$, which is also similar to the $MoSi_2N_4$(MoN) and $MoSi_2N_4$ cases (0.25 and 0.28) [14, 38]. The corresponding 2D stiffness ($C_{\rm 2D}$) of $MoSi_2N_4$(FeN) monolayer is calculated as $C_{\rm 2D} = 2(C_{11} + C_{12}) = 1608$ N/m. Utilizing this value, the gravity-induced out-of-plane deformation (h_d) is estimated as $h_d/L = \sqrt[3]{\rho g L/C_{\rm 2D}}$, where ρ is the density of 2D materials and L is the typical size of samples, which normally adopts $L = 100$ μm [47]. Here, the h_d/L of $MoSi_2N_4$(FeN) monolayer is evaluated to 1.57×10^{-4}, which is similar to the graphene and MoS_2 cases ($\sim 10^{-4}$) [47]. It demonstrates that the $MoSi_2N_4$(FeN) monolayer can well withstand its own weight in the free-standing form. Therefore, combined with the good energetic, dynamical, and thermal stability, the $MoSi_2N_4$(FeN) monolayer is confirmed as a stable 2D system, which will be possibly synthesized by similar methods used for the $MoSi_2N_4$ and $MoSi_2N_4(MoN)_n$ ones.

3.2 Bipolar magnetic semiconducting feature in the $MoSi_2N_4$(FeN) monolayer

Previous study has found that the $MoSi_2N_4$(MoN) system is a nonmagnetic metal [48]. For the $MoSi_2N_4$(FeN) monolayer, we firstly perform a non-spin-polarized calculation on it. As displayed in Fig. S3 of the ESM, there is a narrow band across the Fermi level, which gives rise to a large peak in the density of states (DOSs) at the Fermi level. According to the Stoner theory, a spontaneous spin-polarization will occur in this $MoSi_2N_4$(FeN) monolayer. To this end, a spin-polarized calculation is further conducted, which shows the system becomes magnetic with a total magnetic moment of 1 μ_B/f.u.. The energy gain of the spin-polarization, defined as the energy difference between the nonmagnetic (NM) and ferromagnetic (FM) states, is 0.09 eV/f.u. for the $MoSi_2N_4$(FeN) monolayer. The corresponding spin charge distribution is illustrated in Fig. 2(a), which indicates the magnetism is mainly concentrated on the Fe atoms. This is consistent with the Bader analysis, which shows every Fe atom carries an atomic magnetic moment of 0.97 μ_B. Since the Fe–N–Fe bond angles are close to 90° in the $MoSi_2N_4$(FeN) monolayer, according to the Goodenough-Kanamori-Anderson rule [49], the parallel coupling will be favored between adjacent Fe atoms via the superexchange interactions. To confirm this result, an antiferromagnetic (AFM) state in a $1 \times \sqrt{3}$ supercell is also constructed as shown in Fig. S4 of the ESM. It is found that such AFM state is 0.05 eV/f.u. less stable than the FM one, demonstrating that the system has the FM ground state. The magnetic anisotropy energy (MAE), defined as the energy difference between the systems with the magnetization aligned along the in-plane x and out-of-plane z directions ($\Delta E_{\mathrm{MAE}} = E_{\mathrm{in}} - E_{\mathrm{out}}$), is determined through a non-collinear spin-polarized calculation. The MAE value is obtained to 118 μeV in the $MoSi_2N_4$(FeN) monolayer. We have also compared the energies of systems with the magnetization along the in-plane x and y directions. Their energies are found to be degenerate owing to the in-plane structural isotropy. The positive ΔE_{MAE} value is primarily originated from the hybridization between the d_{xy} and $d_{x^2-y^2}$ orbitals of Fe atom as shown in Fig. 2(b), which manifests the $MoSi_2N_4$(FeN) monolayer has an out-of-plane magnetization. It will lift the Mermin–Wagner restriction and help to maintain a long-range FM order in the 2D system [50]. Thus for the $MoSi_2N_4$(FeN) monolayer, a spin model is further constructed, which adopts a Heisenberg Hamiltonian of $H = -J\sum \boldsymbol{S}_i\boldsymbol{S}_j - A\sum(S_i^z)^2$. Here, J is the nearest-neighbor exchange parameter, A is the anisotropy energy parameter and $\boldsymbol{S}$ is the spin vector at the Fe site, respectively. Since the magnetic moment of Fe atom is close to 1 μ_B, $|\boldsymbol{S}|$ is set to 1, J and A are obtained to 12.5 and 0.118 meV, respectively. The corresponding Monte Carlo (MC) simulation is performed as shown in Fig. 2(a). It can be seen that the magnetization is rapidly decreased to zero in the range of 125–175 K and a specific heat peak appears around 155 K. Thus, based on the Heisenberg model, the estimated Curie temperature (T_C) is about 155 K for the $MoSi_2N_4$(FeN) monolayer, which is larger than the liquid-nitrogen temperature. The T_C of $MoSi_2N_4$(FeN) monolayer is further estimated from the Heisenberg model including the next neighboring couplings. A similar value of 160 K is obtained as shown in Fig. S4 of the ESM, which indicates the next-nearest-neighbor exchange coupling has a negligible effect on the Curie temperature. Similar result has also been found in the monolayer perovskite Rb_2CuCl_4, where the FM exchange is primarily contributed by the nearest-neighbor interaction [51].

The band structures of $MoSi_2N_4$(FeN) monolayer at the FM state are displayed in Figs. 2(c) and (d). It can be seen that PBE calculation shows the $MoSi_2N_4$(FeN) system is a half-metal, while the HSE calculation indicates it is a FM semiconductor. Similar phenomena are also reported in the magnetic $NbSi_2N_4$, VSi_2N_4, and VSi_2P_4 systems, for which the PBE and HSE calculations obtain metallic and semiconducting behaviors, respectively [52]. Such discrepancy between the PBE and HSE results is attributed to that the PBE functional predicts small exchange splitting of d-elements, while the HSE one includes a portion of exact exchange and could better capture it [53]. Here, for the $MoSi_2N_4$(FeN) system, the PBE calculation obtains a small exchange splitting of 1.08 eV for the Fe d_{z^2} orbital. Consequently, the bottom conduction band of spin down electrons is below the Fermi level around the K point. On the other hand, the exchange splitting rises to 4.33 eV in the HSE calculation. The corresponding bottom conduction band is up shifted above the Fermi level and the $MoSi_2N_4$(FeN) system exhibits a semiconducting behavior. It would be noted that the spin up and down bands are staggered around the Fermi level as shown in Fig. 2(d), which is a typical bipolar magnetic feature. The valence band maximum (VBM) and conduction band minimum (CBM) have different spins and they are located at the Γ and K points, respectively. Thus, the $MoSi_2N_4$(FeN) monolayer is an indirect bipolar semiconductor with a band gap of 1.58 eV. The corresponding spin-flip gap in the valence and conduction bands are 0.26 and 0.25 eV, respectively. When the Fermi level moves into these gap regions by electrical gating, a half metal with the controllable polarization direction will be realized [54]. The total and partial DOSs (PDOSs) in Fig. 2(e) indicate the states around the Fermi level are mainly composed of the d states of Fe and Mo atoms. The charge densities of the VBM and CBM in Fig. 2(d) show that the VBM is mainly composed of the Fe d_{z^2} orbital and the N p_z state also makes a small contribution, while the CBM is primarily composed of the Mo d_{z^2} state. Since the

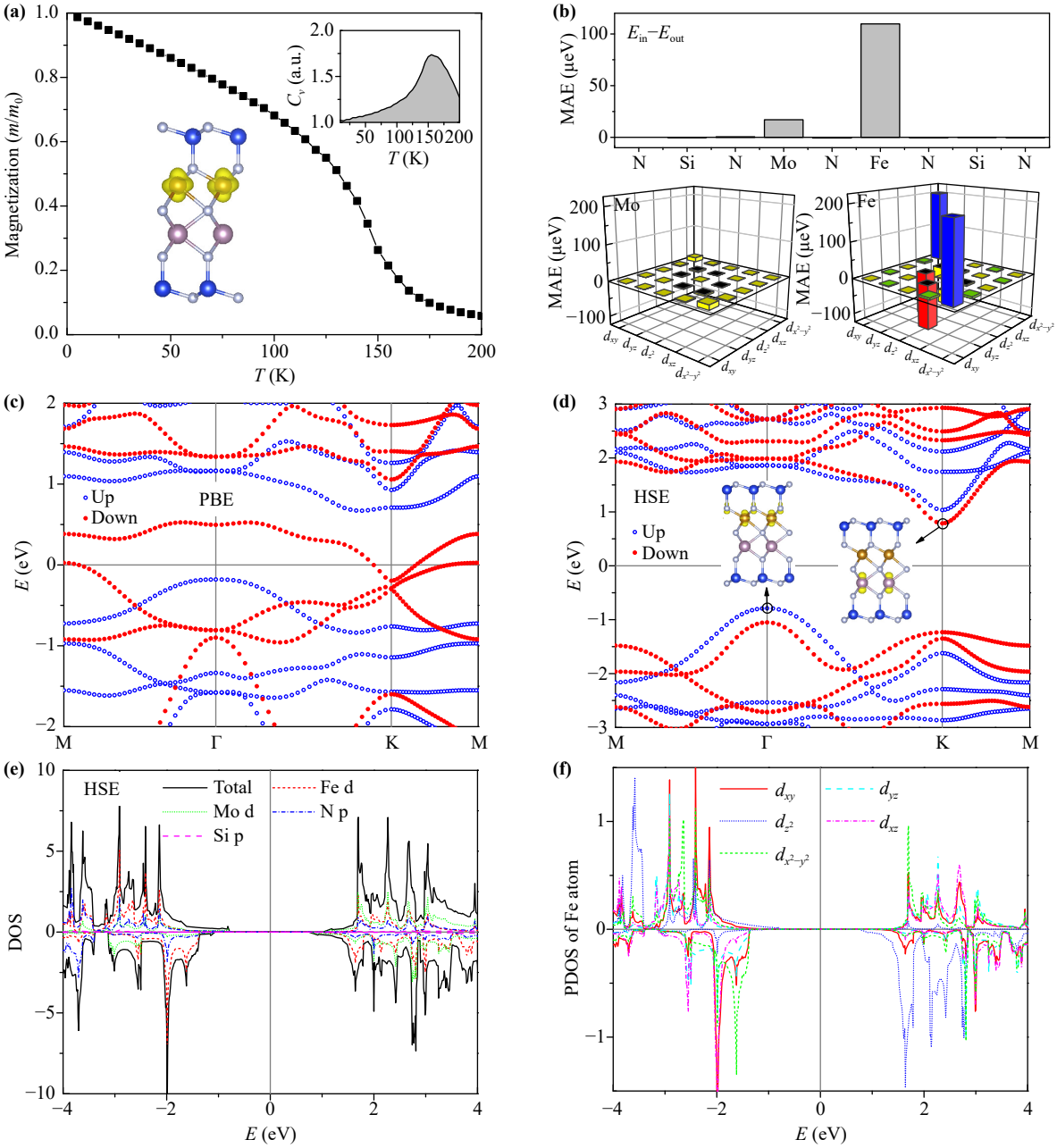

Fig. 2 **(a)** The spin charge density and MC simulation result of the $MoSi_2N_4$(FeN) system, and **(b)** the atomic contributions of its MAE data. The spin-polarized band structures of $MoSi_2N_4$(FeN) monolayer by the **(c)** PBE and **(d)** HSE calculations. **(e)** The total and partial DOSs of $MoSi_2N_4$(FeN) monolayer, and **(f)** the orbital-resolved DOSs for the Fe d orbitals.

magnetism is mainly contributed by the Fe atoms, Fig. 2(f) further depicts the orbital-resolved PDOSs of Fe atoms. It can be seen that among these d orbitals, there is a large spin splitting in the d_{z^2} state, which is occupied for the spin up electrons but nearly empty for the spin down ones. This result is consistent with the spin charge distribution in Fig. 2(a). Through the density derived electrostatic and chemical (DDEC) charge analysis [55], the net atomic charge of Fe atom is obtained as $1.47e$, suggesting that it will have a $+3$ oxidation state with a d^5 electron configuration in the $MoSi_2N_4$(FeN) monolayer. Under the octahedral crystal field, the Fe d orbitals will be split into the triple t_{2g} and double e_g states. Owing to the Janus geometrical structure of system, the FeN_6 octahedron is distorted, which will further split the t_{2g} states into the double e_g^* and single a_{1g} states [56]. The lower e_g^* states are fully occupied by four electrons, and the a_{1g} state is only half filled by one electron, which leads to a net magnetic moment of 1 μ_B/f.u. in this system. The corresponding HSE+SOC band structure is depicted in Fig. S5 of the ESM. It can be seen that the VBM is still located at the

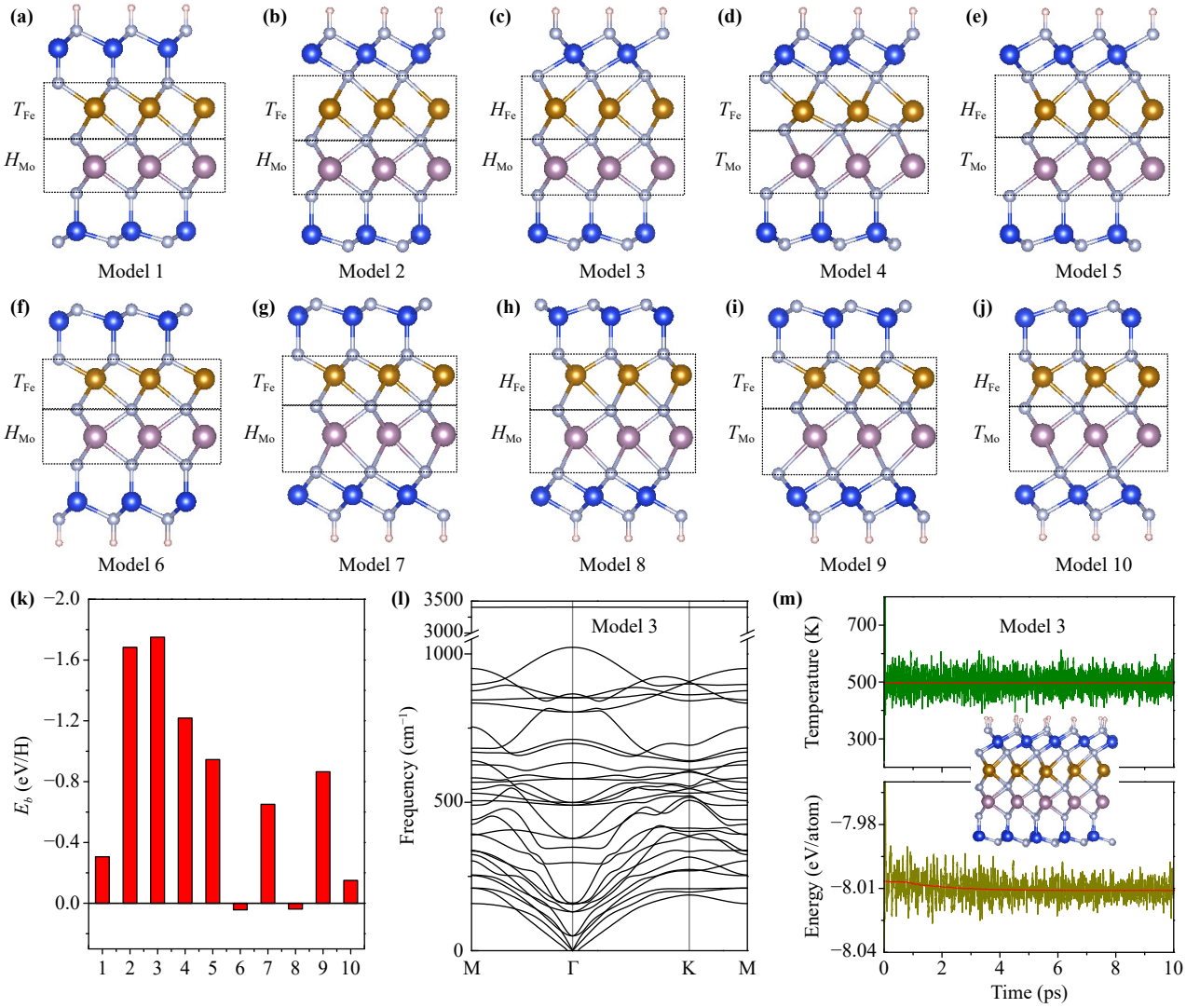

Fig. 3 Model structures of the hydrogenated $MoSi_2N_4$(FeN)H monolayer with the H atoms on the Fe-side **(a–e)** and Mo-side **(f–j)** SiN surface. The octahedral (T) or trigonal-prismatic (H) coordinations for the metal atoms are marked for clarity. **(k)** The E_b of different model structures. **(l)** The phonon dispersions and **(m)** AIMD results of the $MoSi_2N_4$(FeN)H monolayer with the most stable model 3 structure.

Γ point. Although the valley polarization occurs at the K and K′ points in the HSE+SOC calculation, the valley polarization value is merely 0.017 in the bottom conduction band. As a result, the indirect band gap is only slightly reduced by 0.01 eV after the inclusion of SOC effect.

3.3 Geometrical structure of the hydrogenated $MoSi_2N_4$(FeN)H monolayer

For the 2D magnets, surface hydrogenation is an effective strategy to tailor the electronic and magnetic properties, which can enhance magnetic stability and raise the Curie temperature [57, 58]. Since the $MoSi_2N_4$(FeN) monolayer is a Janus structure, the semihydrogenated geometry with hydrogen atoms on one side SiN surface is feasibly formed. For the hydrogenated $MoSi_2N_4$(FeN) system, i.e., the $MoSi_2N_4$(FeN)H one, ten possible geometrical structures are taken into account as shown in Figs. 3(a)–(j). To determine the most stable geometry of $MoSi_2N_4$(FeN)H monolayer, the binding energy (E_b) of H atoms is calculated as $E_b = E_{MoSi_2N_4(FeN)H} - E_{MoSi_2N_4(FeN)} - E_H$. Here $E_{MoSi_2N_4(FeN)H}$ and $E_{MoSi_2N_4(FeN)}$ are the total energies of systems with and without hydrogenation, respectively, and E_H is the atomic energy of an isolated H atom at the spin-polarized state. As shown in Fig. 4, models 1 and 6 have the same H–T stacking structure as the pristine $MoSi_2N_4$(FeN) system, where the H atoms are located on top of the surface N atoms in the upper (Fe-side) and lower (Mo-side) SiN surface, respectively. The corresponding E_b are calculated as –0.31 and 0.04 eV for the models 1 and 6, respectively, suggesting

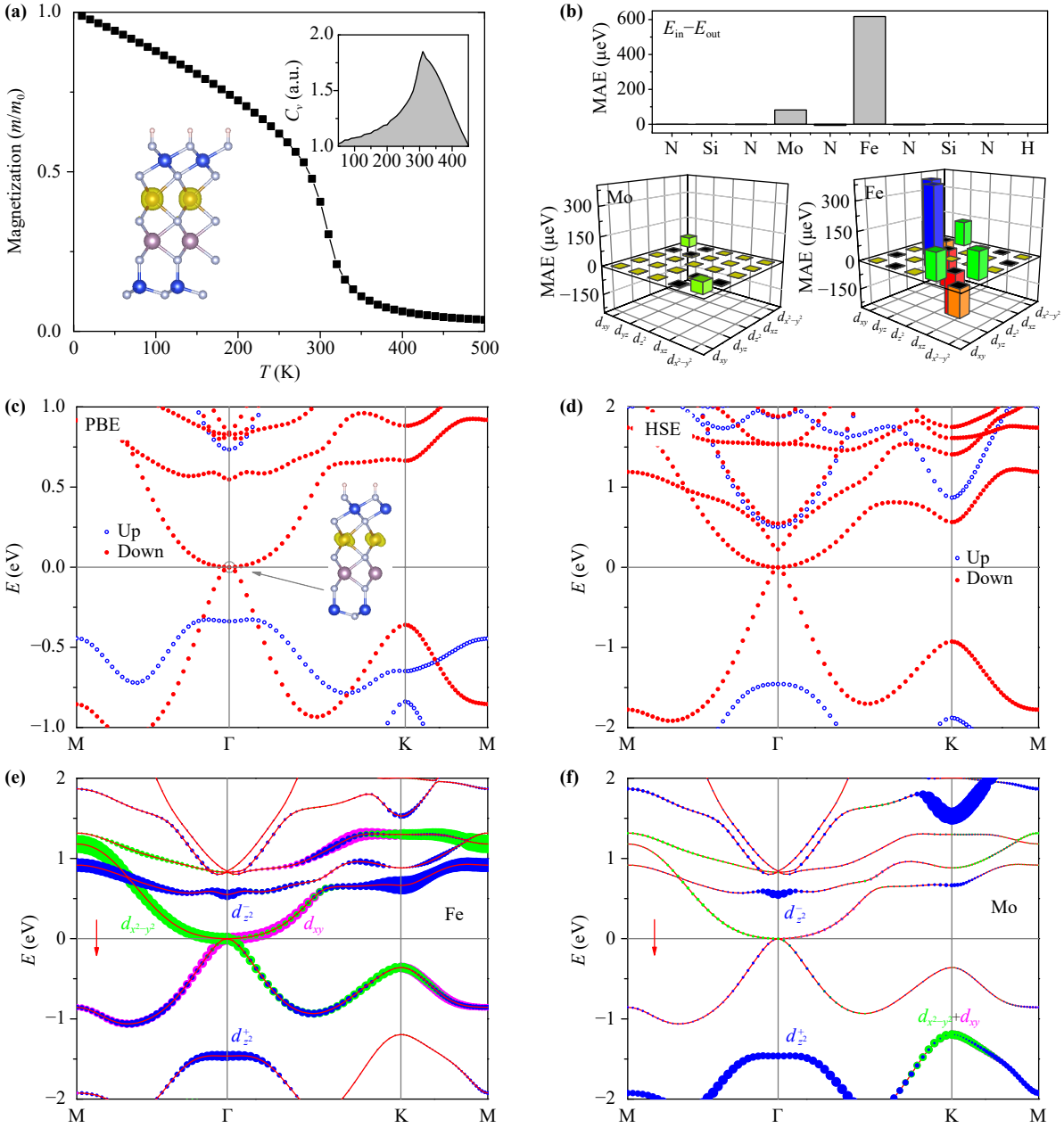

Fig. 4 **(a)** The variations of magnetization and specific heat versus the temperature from the MC simulation on the $MoSi_2N_4$(FeN)H monolayer, and **(b)** the atomic contributions of MAE data in it. The spin charge density of $MoSi_2N_4$(FeN)H monolayer is also displayed in the inset with an isosurface of 0.05 $e/Å^3$. **(c)** PBE and **(d)** HSE band structures of $MoSi_2N_4$(FeN)H monolayer. **(e, f)** The orbital-resolved spin down band structures for Fe and Mo atoms, respectively. Here, the blue, green, and purple dots represent the d_{z^2}, $d_{x^2-y^2}$, and d_{xy} orbitals.

that the Fe-side SiN surface is more easily hydrogenated than the Mo-side one. According to the recent study [59], the surface hydrogenation will induce a structural transformation in the SiN layer. Thus, models 2 and 7 are constructed from models 1 and 6, where the Si atoms in the hydrogenated SiN layer is transformed from a tetrahedral coordination to an octahedral one. It would be noted that the E_b of models 2 and 7 are –1.68 and –0.65 eV/H, much lower than the ones of models 1 and 6. It indicates the transformation in the hydrogenated SiN surface layer will greatly enhance the structural stability of $MoSi_2N_4$(FeN)H monolayer. Based on models 2 and 7, we further enumerate all the possible combinations of the T- and H-phase geometries for the metal atoms. As shown in Fig. 3(k), model 3, where both the Fe and Mo atoms have the trigonal-prismatic H-phase geometry, has the lowest E_b of –1.75 eV/H. It indicates that model 3 is the most stable geometry of

$MoSi_2N_4$(FeN)H monolayer. Similar to the group-V MSi_2N_4 systems [59], the hydrogenation will also induce a structural transformation in the $MoSi_2N_4$(FeN) monolayer, where both the coordinations of Si and metal atoms can be changed by the surface hydrogenation.

In the following, we mainly focus on the most energetically stable structure, i.e., model 3 of the $MoSi_2N_4$(FeN)H monolayer. The structural stability of this system is examined from the mechanical, dynamical and thermal perspectives. The elastic constants are calculated as $C_{11} = 619$ and $C_{12} = 176$ N/m, respectively. These values satisfy the Born–Huang criteria and confirm the mechanical stability. The phonon dispersions are displayed in Fig. 3(l), which shows no soft modes are present in the $MoSi_2N_4$(FeN)H monolayer. The corresponding AIMD simulation results are depicted in Fig. 3(m). It can be seen that the structural integrity is well kept during the AIMD simulation at 500 K, which has no bond breaking in the final configuration. Thus, it can be inferred that the $MoSi_2N_4$(FeN)H monolayer possesses robust structural stability, which is conducive to the experimental synthesis and practical applications.

3.4 Magnetic and electronic properties of the hydrogenated system

Compared to the pristine $MoSi_2N_4$(FeN) system, the hydrogenation raises the total magnetic moment to 4.0 μ_B/f.u.. Every Fe atom carries a larger atomic magnetic moment of 3.41 μ_B in the $MoSi_2N_4$(FeN)H monolayer. Such increase is mainly attributed to the changes of d electron number and coordination of Fe atoms. Utilizing the DDEC charge analysis, the net atomic charge of Fe atom is found to decrease to 1.13 e in the $MoSi_2N_4$(FeN)H system. It suggests the oxidation state of Fe atoms is reduced from +3 to +2, which leads to a d^6 electron configuration in the hydrogenated system. In the $MoSi_2N_4$(FeN)H monolayer, the Fe atoms has a trigonal prismatic coordination, which will split the d orbitals into the singlet d_{z^2} and doubly degenerate d_{xy/x^2-y^2} and $d_{xz/yz}$ states. It is found that there is a remarkable spin splitting in the Fe d states, which is larger than 3 eV from the PBE calculation. Thus, following the Hund's rule, the Fe atoms have a high spin state of $d^{5\uparrow 1\downarrow}$ in the $MoSi_2N_4$(FeN)H monolayer. The spin up Fe d states are fully occupied, while the spin down ones are only partially filled with one d electron, which results in a net magnetic moment of 4 μ_B/f.u., much bigger than that of pristine $MoSi_2N_4$(FeN) system (1 μ_B/f.u.). In addition to the increased magnetic moment, the energetic stability of ferromagnetism is also enhanced. Compared to the AFM order, the FM state is energetically more favourable by 0.10 eV/f.u. in the hydrogenated system, which is twice the value of $MoSi_2N_4$(FeN) monolayer (0.05 eV/f.u.). Moreover, the MAE of $MoSi_2N_4$(FeN)H monolayer also rises to 697 μeV as shown in Fig. 4(b), and the positive MAE mainly stems from the hybridization between Fe d_{yz} and $d_{z^2}/d_{x^2-y^2}/d_{xy}$ orbitals. Since the spin charges are mainly localized on the Fe atoms, a similar Hamiltonian formula is adopted as the pristine system in the MC simulation. The $|S|$ is set to 2, and J and A are adopted to 6.45 and 0.17 meV for the $MoSi_2N_4$(FeN)H system. From the MC simulation result in Fig. 4(a), the estimated Curie temperature of $MoSi_2N_4$(FeN)H monolayer is 310 K around room temperature. Therefore, through the surface hydrogenation, an intriguing room-temperature ferromagnetism emerges in the $MoSi_2N_4$(FeN)H monolayer. Such high T_C value is comparable to the values of $Ru(OH)_2$ (306 K [60]), T-$CrTe_2$ (~300 K [61]), and VS_2 (292 K [62]) monolayers, and is much higher than the experimentally synthesized CrI_3 (45 K [63]), $Cr_2Ge_2Te_6$ (30 K [64]) and Fe_3GeTe_2 (20 K [65]) systems.

More interestingly, different from the pristine $MoSi_2N_4$(FeN) system, the hydrogenated $MoSi_2N_4$(FeN)H monolayer exhibits a spin-gapless semiconducting behavior. Figure 4(c) illustrates the PBE band structure, which shows the spin up bands are semiconducting with an indirect band gap of 1.06 eV. While the spin down bands exhibit a zero-gap characteristic with the top valence and bottom conduction bands touching each other at the Γ point. Similar results are also obtained by the HSE calculation in Fig. 4(d), which shows the gap size in the spin up bands is enlarged to 1.96 eV while the spin down bands still present a spin-gapless feature. Such half-metallic behavior is similar to the Mg_4N_4 system [66], but is different from the $CrSiTe_3$ system, which is a magnetic second-order topological insulator with the semiconducting feature [67]. The orbital-resolved band structures for Fe and Mo atoms are depicted in Figs. 4(e) and (f), respectively. It can be seen that the top valence and bottom conduction bands in the spin down channel are mainly originated from the d_{xy} and $d_{x^2-y^2}$ orbitals of Fe atoms. This is in accordance with the partial charge densities in Fig. 4(c) showing that the degenerate bands at the Γ point are composed of the in-plane d states of Fe atoms.

3.5 Quantum anomalous Hall insulating state in the $MoSi_2N_4$(FeN)H monolayer

It would be noted that when the SOC effect is taken into account, the degeneracy at the Γ point is lifted in the $MoSi_2N_4$(FeN)H monolayer. A local band gap of 0.073 eV is opened at the Γ point as shown in Fig. 5(a). Since the CBM is no longer at the Γ point but is located along the Γ–K line, the global band gap becomes 0.045 eV from the PBE+SOC result. Such gap opening is verified by the HSE+SOC calculation in Fig. 5(b), which obtains a larger local gap of 0.40 eV at the Γ point and a bigger global gap of 0.23 eV in the

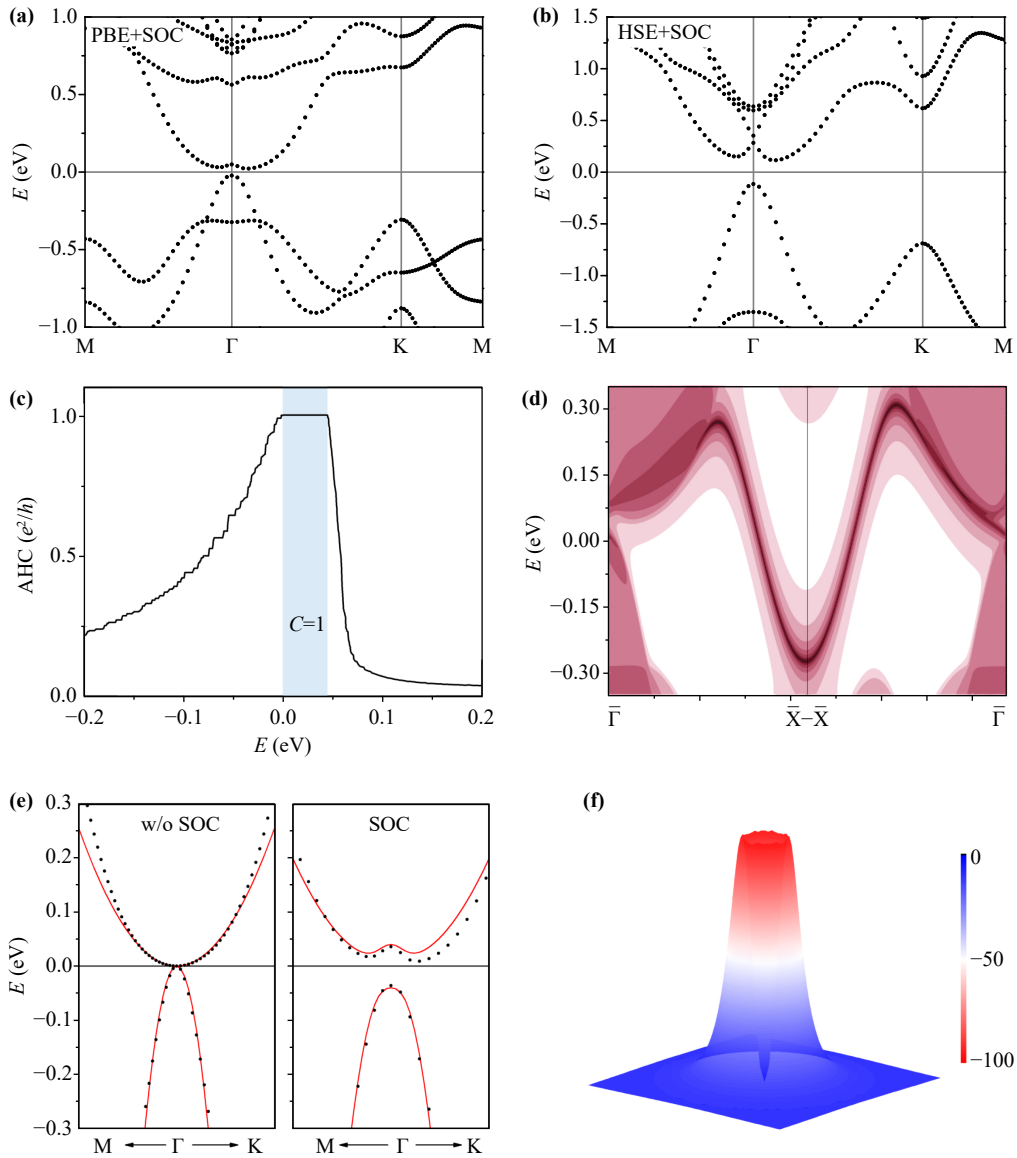

Fig. 5 **(a)** PBE+SOC and **(b)** HSE+SOC band structures of $MoSi_2N_4$(FeN)H monolayer. **(c)** The anomalous Hall conductance and **(d)** edge state of $MoSi_2N_4$(FeN)H monolayer. **(e)** The low-energy band structures without and with the SOC effect. The dots represent the data from the first-principles calculation and the lines stand for the result from the model Hamiltonian. **(f)** The berry curvature of $MoSi_2N_4$(FeN)H monolayer around the Γ point from the model Hamiltonian.

$MoSi_2N_4$(FeN)H system. Such a SOC-induced band gap suggests the system will possess a nontrivial topological feature. To this end, a wannier interpolation is carried out on the PBE+SOC result and the anomalous Hall conductivity (AHC) is calculated as shown in Fig. 6(c). Here, the AHC value is related to the Chern number (C) from the formula of $\sigma_{xy} = C\frac{e^2}{h}$. The Chern number can be directly calculated by integrating the Berry curvature $\Omega(k)$ over the first Brillouin zone as

$$C = \frac{1}{2\pi}\int_{\mathrm{BZ}} \Omega(k)\mathrm{d}^2k,$$

$$\Omega(k) = \sum_n f_n \sum_{n'\neq n} \frac{2\mathrm{Im}\,\langle\Psi_{nk}|\nu_x|\Psi_{n'k}\rangle\,\langle\Psi_{n'k}|\nu_y|\Psi_{nk}\rangle}{E_{n'}^2 - E_n^2},$$

where n is the band index, E_n and Ψ_{nk} are the eigenvalue and eigenstate of band n, ν_x and ν_y are the operator components along the x and y directions, and $f_n = 1$ for all the occupied bands below the Fermi level [68, 69]. As displayed in Fig. 5(c), there is a quantized plateau of 1 e^2/h when the Fermi level lies in the gap region. Thus the $MoSi_2N_4$(FeN)H monolayer has a nonzero Chern number of $C = 1$, which is similar to the Nb_2O_3 one [70, 71]. This manifests the system will be an intriguing quantum anomalous Hall insulator. The corresponding

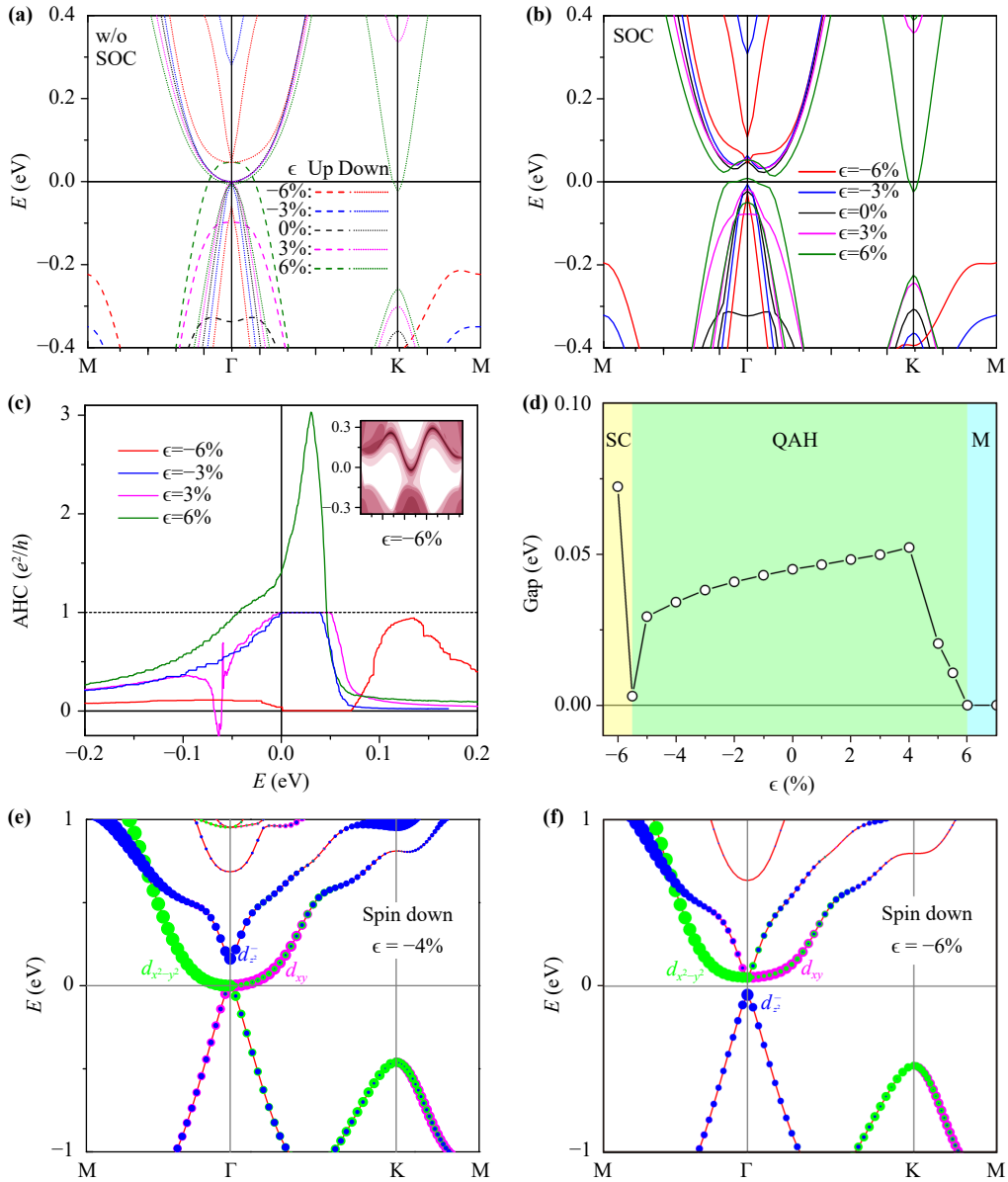

Fig. 6 **(a, b)** The band structures of $MoSi_2N_4$(FeN)H monolayer under strains of $\epsilon = -6\%$, -3%, 0%, 3% and 6% without and with SOC effect. **(c)** The corresponding anomalous Hall conductance of $MoSi_2N_4$(FeN)H monolayer under different strains. **(d)** The global band gap of system as a function of strain from the PBE+SOC calculations. **(e, f)** A comparison of orbital-resolved spin down band structures at the compressive strains of $\epsilon = -4\%$ and -6%, respectively. For clarity, only the orbitals related to the band inversion are displayed.

edge state is further evaluated by the iterative Green function method in Fig. 5(d). Clearly, there is one edge state connecting the valence and conduction bands in the bulk gap, which is consistent with the $C = 1$ result.

Such nontrivial topology is closely related to the existence of d–d band inversion. In the $MoSi_2N_4$(FeN)H monolayer, both the Fe and Mo atoms have the trigonal prismatic coordination, which will split their d states into the singlet d_{z^2} and doubly degenerate d_{xy/x^2-y^2} and $d_{xz/yz}$ states. Normally, the energies of these states follow the order of $E(d_{z^2}) < E(d_{xy/x^2-y^2}) < E(d_{xy/yz})$ under the trigonal prismatic crystal field [72]. Since the Fe and Mo atoms face each other directly in the $MoSi_2N_4$(FeN)H monolayer, their d_{z^2} states will hybridize with each other, forming the bonding $d_{z^2}^+$ and antibonding $d_{z^2}^-$ ones. As shown in Figs. 5(e) and (f), the antibonding $d_{z^2}^-$ state is located above the d_{xy/x^2-y^2} ones, which is in sharp contrast to the normal order of these d orbitals. It demonstrates that there is a d–d band inversion in the $MoSi_2N_4$(FeN)H monolayer, which is responsible for the appearance of the nontrivial topological characteristic. Such band inversion between d_{xy/x^2-y^2} and d_{z^2} orbitals has also been reported in the H-phase RuClBr monolayer, which exhibits a quantum anomalous valley

Hall effect [73].

To get more insights into the QAH behavior, the $\boldsymbol{k}\cdot\boldsymbol{p}$ method is used to construct a two-band model for the $MoSi_2N_4$(FeN)H monolayer. According to the band components of band edges, the basis sets are chosen as $|d_{+,\uparrow}\rangle$, $|d_{-,\uparrow}\rangle$, $|d_{+,\downarrow}\rangle$, and $|d_{-,\downarrow}\rangle$ with $|d_{\pm}\rangle = \frac{1}{\sqrt{2}}(d_{xy} \pm \mathrm{i}d_{x^2-y^2})$ and $\uparrow$ ($\downarrow$) representing the spin up (down) state. Note that when the magnetic interactions and SOC effect are ignored, the time-reversal symmetry and the threefold rotation symmetry (C_{3v}) are preserved. Therefore the low-energy effective Hamiltonian takes a block diagonalized form of

$$H_0 = \begin{pmatrix} \varepsilon_1(k)+\epsilon & f(k) & 0 & 0 \\ f*(k) & \varepsilon_2(k)+\epsilon & 0 & 0 \\ 0 & 0 & \varepsilon_1(k)+\epsilon & f(k) \\ 0 & 0 & f*(k) & \varepsilon_2(k)+\epsilon \end{pmatrix},$$

where $f(k)$ is the hopping matrix element, which is an even function of k and takes the form of $f(k) = bk_-^2$ with $k_\pm = k_x \pm \mathrm{i}k_y$ due to the constraints of time-reversal symmetry and C_{3v} crystal symmetry. Similarly, $\varepsilon_1(k) = \varepsilon_2(k) = ak^2$ with $k = |k|$ due to the symmetry constraints [74]. ϵ is a correction energy relevant to the Fermi energy. When the magnetic interactions are considered, the exchange term can be expressed as $H_{\mathrm{ex}} = -m\sigma_z \otimes I_2$, where σ_z is the Pauli matrix and m represents the effective exchange splitting between the spin up and down states, and I_2 is the 2×2 identity matrix. For the SOC effect, the additional term is $H_{\mathrm{SOC}} = \lambda_{so} S\cdot L$, which has a diagonalized form of $H_{\mathrm{SOC}} = \lambda_{so}\mathrm{diag}[1,-1,-1,1]$ in the chosen basis sets. Since the spin up Fe d states are far away the Fermi level, only the spin down ones dominate the low-energy physics of system. Thus, we can focus on the spin down channel under the basis sets of $|d_{+,\downarrow}\rangle$ and $|d_{-,\downarrow}\rangle$, and combining the three terms of H_0, H_{ex}, and H_{SOC}, the total Hamiltonian is

$$H(k,\downarrow) = \begin{pmatrix} ak^2+\epsilon+m-\lambda_{so} & bk_-^2 \\ bk_+^2 & ak^2+\epsilon+m+\lambda_{so} \end{pmatrix}.$$

Through solving the Hamiltonian, the eigenvalues are obtained as $E_\pm(k) = (ak^2+\epsilon+m) \pm \sqrt{b^2k^4+\lambda_{so}^2}$. When the SOC effect is neglected, we have $E_\pm(k) = (a\pm b)k^2+\epsilon+m$. Since the Fermi level is adopted to 0 eV, the constants of $\epsilon+m$ will be set to zero. Thus, both $E_+(k)$ and $E_-(k)$ exhibit a quadratic dispersion with k, which are degenerate at the Γ point, consistent with first-principles calculations. When the SOC effect is taken into account, a finite λ_{SOC} will lift the degeneracy of $E_+(k)$ and $E_-(k)$ and opens a band gap of $2\lambda_{\mathrm{SOC}}$ at the Γ point. Through fitting the $E_\pm(k)$ expressions to the PBE and PBE+SOC results, the parameters are obtained as a = –3.66 eV·Å^2, b = 4.45 eV·Å^2, and λ_{so} = 0.036 eV, respectively. From Fig. 5(e), it can be seen that the $\boldsymbol{k}\cdot\boldsymbol{p}$ model can capture the main physics of $MoSi_2N_4$(FeN)H monolayer around the Γ point. Owing to the dissimilar electronic property, such $\boldsymbol{k}\cdot\boldsymbol{p}$ model is inapplicable to the trivial $MoSi_2N_4$(FeN) one. According to the Hamiltonian, the Berry curvature can be analytically obtained as $\Omega(k) = -\frac{2b^2\lambda_{so}k^2}{\sqrt{(b^2k^4+\lambda_{so}^2)^3}}$. As displayed in Fig. 6(f), the Berry curvature is nonzero around the Γ point. Using the $\Omega(k)$ expression, the Chern number for the spin down states can be obtained as $C_\downarrow = \frac{1}{2\pi}\int_{BZ}\Omega(k)\mathrm{d}^2k = -1$. With the time-reversal symmetry, we will have $C_\uparrow = -C_\downarrow = 1$. The spin Chern number of system, defined as the half difference between Chern numbers of spin up and down states [75], is calculated as $C = 1/2(C_\uparrow - C_\downarrow) = 1$ for the $MoSi_2N_4$(FeN)H system. This result agrees well with the first-principles data and proves the nontrivial topological character of the $MoSi_2N_4$(FeN)H monolayer.

Finally, we investigate the strain effects on the nontrivial topological feature of $MoSi_2N_4$(FeN)H monolayer. Homogeneous in-plane strain is applied to the system as $\epsilon = (a-a_0)/a_0 \times 100\%$, where a and a_0 are the lattice constants with and without strain, respectively. As shown in Figs. 6(a) and (b), under the tensile strains, the top valence and bottom conduction bands always touch each other at the Γ point. The SOC effect opens a nontrivial band gap, which maintains the intriguing QAH state in the stretched $MoSi_2N_4$(FeN)H monolayer. It would be noted that the conduction band edge at the K point is declined by the tensile strain and drops below the Fermi level when $\epsilon \geq 6\%$. Although there is still a local band gap at the Γ point, the global band gap is closed as shown in Fig. 6(b). Thus the $MoSi_2N_4$(FeN)H monolayer is converted into a metal under large tensile strains of $\epsilon \geq 6\%$. On the other hand, when the compressive strain is applied, the QAH state is preserved until $\epsilon = -5\%$. Then, the global gap is decreased rapidly to zero around $\epsilon = -5.5\%$ and reopened again at $\epsilon = -6\%$. Such band gap variation is closely related to the change of band components of band edges. For the $MoSi_2N_4$(FeN)H monolayer, the $d_{z^2}^-$ state at the Γ point is always located above the $d_{xy}/d_{x^2-y^2}$ ones for the Fe atoms when the strain $\epsilon > -5\%$, demonstrating that the d–d band inversion is preserved in the $MoSi_2N_4$(FeN)H monolayer. Because the compressive strain raises the distance between the Fe and Mo atoms, the hybridization between them will be will weakened, which causes the down shift of $d_{z^2}^-$ state. Figure 6(e) depicts the orbital-resolved spin down band structure of system under a compressive strain of $\epsilon = -4\%$. It can be seen that the $d_{z^2}^-$ state is still above the $d_{xy}/d_{x^2-y^2}$ ones although the energy difference between them is decreased from 0.55 eV under the strain-free state to 0.16 eV under the strain of $\epsilon = -4\%$. When the compressive strain exceeds –5%, the $d_{z^2}^-$ state is moved below the $d_{xy}/d_{x^2-y^2}$ ones, which diminishes the band inversion and causes a direct band gap at the Γ point even without the SOC effect. This could be clearly visualized from the orbital-resolved

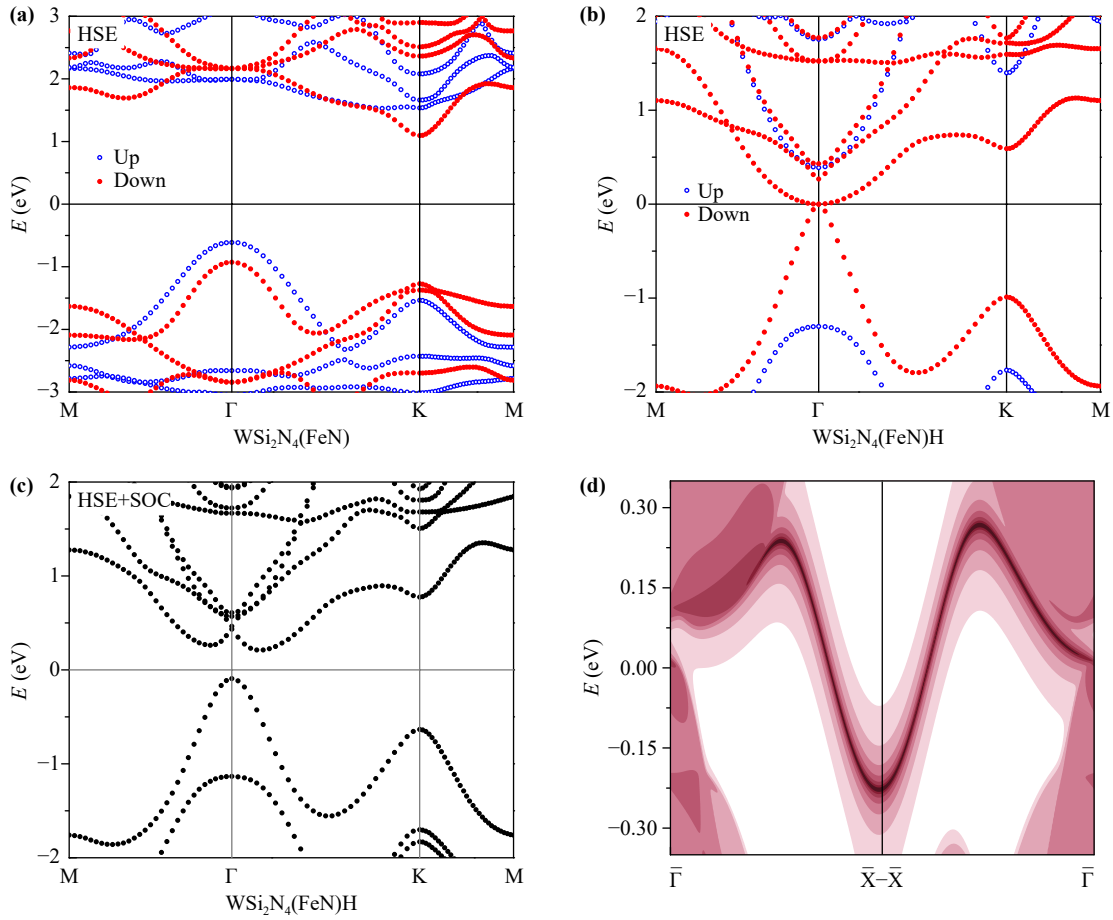

Fig. 7 **(a)** The HSE band structure of WSi_2N_4(FeN) monolayer. **(b)** The HSE and **(c)** HSE+SOC band structures of WSi_2N_4(FeN)H system. **(d)** The corresponding edge state calculation on the WSi_2N_4(FeN)H monolayer.

spin down band structure of system at $\epsilon = -6\%$ in Fig. 6(f). Accompanied with the disappearance of d–d band inversion, the compressed $MoSi_2N_4$(FeN)H monolayer undergoes a nontrivial-to-trivial topological phase transition. As displayed in Fig. 6(c), the quantized plateau and edge states disappear, manifesting the system becomes a trivial FM semiconductor at $\epsilon = -6\%$. Thus, a nontrivial-to-trivial phase transition will be induced in the $MoSi_2N_4$(FeN)H monolayer under large compressive strains. It would be noted that for the free-standing 2D materials, the basal plane will tend to buckle under large compressive strains. In the experiment, such buckling could be effectively suppressed by enhancing the interfacial strength between the film and substrate or the reinforcement of the film rigidity [76]. Since the $MoSi_2N_4$(FeN)H monolayer is a rigid system with the large Young's modulus, when it is supported on a suitable substrate with enough interfacial adhesion, the buckling will be suppressed in the strained system. The QAH insulating state in $MoSi_2N_4$(FeN)H system is robust against homogeneous strains within a wide range of [–5%, 5%], which is advantageous for practical applications. In the experiment, external strains have been realized on 2D systems by several methods, such as bending, rolling, elongation, thermal expansion, and piezoelectric gating techniques [77, 78]. Large strains (>10%) have already been applied on the graphene, MoS_2 and BN monolayers [77, 78], and for the $MoSi_2N_4$(FeN)H monolayer, the moderate strains (≤6%) will be possibly realized using similar approaches.

3.6 The electronic and topological properties of W-based analogues

In addition to the $MoSi_2N_4$(FeN) and $MoSi_2N_4$(FeN)H monolayers, the corresponding W-based analogues are also investigated. For the WSi_2N_4(FeN) monolayer, it still prefers the FM state and presents a bipolar magnetic semiconducting feature. As shown in Fig. 7(a), the VBM is located at the Γ point in the spin up channel, while the CBM lies at the K point in the spin down channel instead. The indirect gap size is 1.70 eV and the spin-flip gap in the valence and conduction bands are 0.32 and 0.44 eV, respectively, which are both larger than the values of $MoSi_2N_4$(FeN) system. Upon the hydrogenation, the ferromagnetism is also enhanced in

the WSi_2N_4(FeN) monolayer, whose total magnetic moment is increased from 1 to 4 μ_B/f.u. and the Curie temperature T_C is raised to 660 K. Just like the $MoSi_2N_4$(FeN)H system, the hydrogenated WSi_2N_4(FeN)H monolayer exhibits a spin-gapless behaviour without the SOC effect. As shown in Fig. 7(b), the spin up bands are semiconducting while the spin down ones are gapless with the top valence and bottom conduction bands touching each other at the Γ point. When the SOC effect is taken into account, a nontrivial gap is opened as shown in Fig. 7(c). Owing to the heavier W element, the local band gap at the Γ point is up to 0.52 eV and the global band gap in the whole Brillouin zone becomes 0.31 eV, which is bigger than the $MoSi_2N_4$(FeN)H one. The nontrivial topological feature of WSi_2N_4(FeN)H monolayer is analyzed from the edge states in Fig. 7(d). It can be seen that there is one edge state in the bulk gap, which links the conduction bands in the $\overline{\Gamma}$–$\overline{X}$ line and touches the valence bands in the $-\overline{X}$–$\overline{\Gamma}$ line. Such asymmetric behavior manifests the $E(-k)$ values are no longer equivalent to the $E(k)$ ones in the QAH state, which stems from broken time-reversal symmetry and SOC effect [26]. Considering that the nontrivial band gap and the Curie temperature are both larger than the normal thermal fluctuation energy ($k_BT \approx 0.026$ eV at 300 K), the WSi_2N_4(FeN)H monolayer will be a promising material to realize the room-temperature quantum anomalous Hall effect.

4 Conclusion

In summary, motivated by the recent synthesis of $MoSi_2N_4(MoN)_n$ compounds, we conduct a first-principles study on the electronic, magnetic and topological properties of $MoSi_2N_4$(FeN) system. Such $MoSi_2N_4$(FeN) monolayer is a cousin of $MoSi_2N_4$(MoN) and is composed of overlapped MoN and FeN layers sandwiched between the SiN layers. It is found that (i) heterogeneous metal atoms have different coordinations in the $MoSi_2N_4$(FeN) system, which forms H-phase and T-phase geometries for the MoN_2 and FeN_2 parts, respectively. Robust structural stability is confirmed in the $MoSi_2N_4$(FeN) monolayer from the energetic, mechanical, dynamical and thermal perspectives. (ii) Different from the $MoSi_2N_4$(MoN) system, the $MoSi_2N_4$(FeN) monolayer possesses intrinsic ferromagnetism and presents a bipolar magnetic semiconducting behaviour. The ferromagnetism can be further enhanced by the surface hydrogenation, which will raise the Curie temperature to 310 K around room temperature. (iii) More importantly, the hydrogenated $MoSi_2N_4$(FeN)H system becomes an intriguing quantum anomalous Hall insulator with a sizeable band gap of 0.23 eV. The nontrivial topological character can be well described by a two-band $\boldsymbol{k}\cdot\boldsymbol{p}$ model, which confirms a nonzero Chern number of $C = 1$. The QAH insulating state is robust against strains, which is preserved in a wide range of [–5%, 5%]. (iv) Similar behaviours are present in the W-based counterparts, where the pristine WSi_2N_4(FeN) monolayer is a bipolar magnetic semiconductor and the hydrogenated WSi_2N_4(FeN)H one will be a promising room-temperature quantum anomalous Hall insulator. Our study demonstrates that as a member of newly discovered $MA_2Z_4(MN)_n$ family materials, the double transition-metal MSi_2N_4(FeN) systems will be a fertile platform to achieve fascinating spintronic and topological properties.

Declarations The authors declare that they have no competing interests and there are no conflicts.

Electronic supplementary materials The online version contains supplementary material available at https://doi.org/10.1007/s11467-024-1431-6 and https://journal.hep.com.cn/fop/EN/10.1007/s11467-024-1431-6.

Acknowledgements The authors acknowledge the support from the National Natural Science Foundation of China (No. 11774312).

References

1. Y. L. Hong, Z. Liu, L. Wang, T. Zhou, W. Ma, C. Xu, S. Feng, L. Chen, M. L. Chen, D. M. Sun, X. Q. Chen, H. M. Cheng, and W. Ren, Chemical vapor deposition of layered two-dimensional $MoSi_2N_4$ materials, *Science* 369(6504), 670 (2020)
2. Y. Yin, Q. Gong, M. Yi, and W. Guo, Emerging versatile two-dimensional $MoSi_2N_4$ family, *Adv. Funct. Mater.* 33(26), 2214050 (2023)
3. C. C. Tho, S. D. Guo, S. J. Liang, W. L. Ong, C. S. Lau, L. Cao, G. Wang, and Y. S. Ang, MA_2Z_4 family heterostructures: Promises and prospects, *Appl. Phys. Rev.* 10(4), 041307 (2023)
4. D. Huang, F. Liang, R. Guo, D. Lu, J. Wang, H. Yu, and H. Zhang, $MoSi_2N_4$: A 2D regime with strong exciton –phonon coupling, *Adv. Opt. Mater.* 10(9), 2102612 (2022)
5. K. S. Novoselov, Discovery of 2D van der Waals layered $MoSi_2N_4$ family, *Natl. Sci. Rev.* 7(12), 1842 (2020)
6. B. Mortazavi, B. Javvaji, F. Shojaei, T. Rabczuk, A. V. Shapeev, and X. Zhuang, Exceptional piezoelectricity, high thermal conductivity and stiffness and promising photocatalysis in two-dimensional $MoSi_2N_4$ family confirmed by first-principles, *Nano Energy* 82, 105716 (2021)
7. S. Li, W. Wu, X. Feng, S. Guan, W. Feng, Y. Yao, and S. A. Yang, Valley-dependent properties of monolayer $MoSi_2N_4$, WSi_2N_4, and $MoSi_2As_4$, *Phys. Rev. B* 102(23), 235435 (2020)
8. C. Yang, Z. Song, X. Sun, and J. Lu, Valley pseudospin in monolayer $MoSi_2N_4$ and $MoSi_2As_4$, *Phys. Rev. B* 103(3), 035308 (2021)
9. Y. Wu, Z. Tang, W. Xia, W. Gao, F. Jia, Y. Zhang, W. Zhu, W. Zhang, and P. Zhang, Prediction of protected

band edge states and dielectric tunable quasiparticle and excitonic properties of monolayer $MoSi_2N_4$, *npj Comput. Mater.* 8(1), 129 (2022)
10. J. Yu, J. Zhou, X. Wan, and Q. Li, High intrinsic lattice thermal conductivity in monolayer $MoSi_2N_4$, *New J. Phys.* 23(3), 033005 (2021)
11. X. Wang, W. Ju, D. Wang, X. Li, and J. Wan, Flexible MA_2Z_4 (M = Mo, W; A = Si, Ge and Z = N, P, As) monolayers with outstanding mechanical, dynamical, electronic, and piezoelectric properties and anomalous dynamic polarization, *Phys. Chem. Chem. Phys.* 25(27), 18247 (2023)
12. A. Priydarshi, Y. S. Chauhan, S. Bhowmick, and A. Agarwal, Large and anisotropic carrier mobility in monolayers of the MA_2Z_4 series (M = Cr, Mo, W; A = Si, Ge; and Z = N, P), *Nanoscale* 14(33), 11988 (2022)
13. L. Wang, Y. Shi, M. Liu, A. Zhang, Y. L. Hong, R. Li, Q. Gao, M. Chen, W. Ren, H. M. Cheng, Y. Li, and X. Q. Chen, Intercalated architecture of MA_2Z_4 family layered van der Waals materials with emerging topological, magnetic and superconducting properties, *Nat. Commun.* 12(1), 2361 (2021)
14. Y. Ding and Y. Wang, Computational exploration of stable $4d/5d$ transition-metal MSi_2N_4 (M = Y–Cd and Hf–Hg) nanosheets and their versatile electronic and magnetic properties, *J. Phys. Chem. C* 125(35), 19580 (2021)
15. Y. T. Ren, L. Hu, Y. T. Chen, Y. J. Hu, J. L. Wang, P. L. Gong, H. Zhang, L. Huang, and X. Q. Shi, Two-dimensional MSi_2N_4 monolayers and van der Waals heterostructures: Promising spintronic properties and band alignments, *Phys. Rev. Mater.* 6(6), 064006 (2022)
16. Y. Wang, D. Legut, X. Liu, Y. Li, C. Li, Y. Sun, R. Zhang, and Q. Zhang, Mott transition and superexchange mechanism in magnetically doped XSi_2N_4 caused by large $3d$ orbital onsite coulomb interaction, *Phys. Rev. B* 106(10), 104421 (2022)
17. Z. An, L. Lv, Y. Su, Y. Jiang, and Z. Guan, Carrier doping modulates the magnetoelectronic and magnetic anisotropic properties of two-dimensional MSi_2N_4 (M = Cr, Mn, Fe, and Co) monolayers, *Phys. Chem. Chem. Phys.* 26(5), 4208 (2024)
18. Q. Cui, Y. Zhu, J. Liang, P. Cui, and H. Yang, Spin-valley coupling in a two-dimensional VSi_2N_4 monolayer, *Phys. Rev. B* 103(8), 085421 (2021)
19. S. Li, Q. Wang, C. Zhang, P. Guo, and S. A. Yang, Correlation-driven topological and valley states in monolayer VSi_2P_4, *Phys. Rev. B* 104(8), 085149 (2021)
20. Y. Wang and Y. Ding, Switchable valley polarization and quantum anomalous Hall state in the $VN_2X_2Y_2$ nanosheets (X = group-III and Y = group-VI elements), *Appl. Phys. Lett.* 119(19), 193101 (2021)
21. P. Liu, S. Liu, M. Jia, H. Yin, G. Zhang, F. Ren, B. Wang, and C. Liu, Strain-driven valley states and phase transitions in Janus $VSiGeN_4$ monolayer, *Appl. Phys. Lett.* 121(6), 063103 (2022)
22. P. Li, X. Yang, Q. S. Jiang, Y. Z. Wu, and W. Xun, Built-in electric field and strain tunable valley-related multiple topological phase transitions in $VSiXN_4$ (X = C, Si, Ge, Sn, Pb) monolayers, *Phys. Rev. Mater.* 7(6), 064002 (2023)
23. K. Jia, X. J. Dong, S. S. Li, W. X. Ji, and C. W. Zhang, Strain-engineering induced topological phase transitions and multiple valley states in Janus monolayer $VCSiN_4$, *J. Mater. Chem. C* 11(30), 10359 (2023)
24. Z. Gao, Y. He, and K. Xiong, Two-dimensional Janus $SVAN_2$ (A = Si, Ge) monolayers with intrinsic semiconductor character and room temperature ferromagnetism: Tunable electronic properties via strain and an electric field, *Dalton Trans.* 52(46), 17416 (2023)
25. X. Zhou, R. W. Zhang, Z. Zhang, W. Feng, Y. Mokrousov, and Y. Yao, Sign-reversible valley-dependent berry phase effects in 2D valley-half-semiconductors, *npj Comput. Mater.* 7(1), 160 (2021)
26. C. Z. Chang, C. X. Liu, and A. H. MacDonald, Colloquium: Quantum anomalous Hall effect, *Rev. Mod. Phys.* 95(1), 011002 (2023)
27. K. Wang, Y. Li, H. Mei, P. Li, and Z. X. Guo, Quantum anomalous Hall and valley quantum anomalous Hall effects in two-dimensional d_0 orbital XY monolayers, *Phys. Rev. Mater.* 6(4), 044202 (2022)
28. P. Li, Prediction of intrinsic two dimensional ferromagnetism realized quantum anomalous Hall effect, *Phys. Chem. Chem. Phys.* 21(12), 6712 (2019)
29. H. P. Wang, W. Luo, and H. J. Xiang, Prediction of high-temperature quantum anomalous Hall effect in two-dimensional transition-metal oxides, *Phys. Rev. B* 95(12), 125430 (2017)
30. P. Li, X. Li, W. Zhao, H. Chen, M. X. Chen, Z. X. Guo, J. Feng, X. G. Gong, and A. H. MacDonald, Topological Dirac states beyond π-orbitals for silicene on SiC(0001) surface, *Nano Lett.* 17(10), 6195 (2017)
31. Y. Ding and Y. Wang, Two-dimensional T′ MA_2N_4 (M = Mo/W, A = Si/Ge) nanosheets: First-principles insights into the structural stability, electronic property and catalytic performance for hydrogen evolution reaction, *Appl. Surf. Sci.* 627, 157256 (2023)
32. R. Islam, R. Verma, B. Ghosh, Z. Muhammad, A. Bansil, C. Autieri, and B. Singh, Switchable large-gap quantum spin Hall state in the two-dimensional MSi_2Z_4 class of materials, *Phys. Rev. B* 106(24), 245149 (2022)
33. R. Islam, G. Hussain, R. Verma, M. S. Talezadehlari, Z. Muhammad, B. Singh, and C. Autieri, Fast electrically switchable large gap quantum spin Hall states in MGe_2Z_4, *Adv. Electron. Mater.* 9(8), 2300156 (2023)
34. X. Wei, B. Zhao, J. Zhang, Y. Xue, Y. Li, and Z. Yang, Chern insulators without band inversion in MoS_2 monolayers with $3d$ adatoms, *Phys. Rev. B* 95(7), 075419 (2017)
35. X. Deng, H. Yang, S. Qi, X. Xu, and Z. Qiao, Quantum anomalous Hall effect and giant Rashba spin–orbit splitting in graphene system Co-doped with boron and $5d$ transition-metal atoms, *Front. Phys.* 13(5), 137308 (2018)
36. M. A. Abdelati, A. A. Maarouf, and M. M. Fadlallah, Substitutional transition metal doping in $MoSi_2N_4$ monolayer: Structural, electronic and magnetic properties, *Phys. Chem. Chem. Phys.* 24(5), 3035 (2022)
37. Y. Wang, G. Wang, M. Huang, Z. Luo, J. Wang, Z. Ding, X. Guo, and X. Liu, Electrocatalytic activity of $MoSi_2N_4$ monolayers decorated with single transition metal atoms: A computational study, *Nanotechnology*

34(24), 245705 (2023)
38. Z. Liu, L. Wang, Y. L. Hong, X. Q. Chen, H. M. Cheng, and W. Ren, Two-dimensional superconducting $MoSi_2N_4(MoN)_{4n}$ homologous compounds, *Natl. Sci. Rev.* 10(4), nwac273 (2023)
39. Y. Wang and Y. Ding, Large-gap quantum spin hall state in double-transition-metal homologous compounds of WSi_2N_4: A first-principles study, *Phys. Status Solidi Rapid Res. Lett.* 18(3), 2300376 (2024)
40. A. Miura, K. Tadanaga, E. Magome, C. Moriyoshi, Y. Kuroiwa, T. Takahiro, and N. Kumada, Octahedral and trigonal-prismatic coordination preferences in Nb-, Mo-, Ta-, and W-based ABX_2 layered oxides, oxynitrides, and nitrides, *J. Solid State Chem.* 229, 272 (2015)
41. E. Enriquez, Y. Zhang, A. Chen, Z. Bi, Y. Wang, E. Fu, Z. Harrell, X. Lu, P. Dowden, H. Wang, C. Chen, and Q. Jia, Epitaxial growth and physical properties of ternary nitride thin films by polymer-assisted deposition, *Appl. Phys. Lett.* 109(8), 081907 (2016)
42. G. Kresse and J. Furthmuller, Efficiency of *ab-initio* total energy calculations for metals and semiconductors using a plane-wave basis set, *Comput. Mater. Sci.* 6(1), 15 (1996)
43. G. C. Moore, M. K. Horton, E. Linscott, A. M. Ganose, M. Siron, D. D. O'Regan, and K. A. Persson, High-throughput determination of Hubbard U and Hund J values for transition metal oxides via the linear response formalism, *Phys. Rev. Mater.* 8(1), 014409 (2024)
44. R. Panda and N. Gajbhiye, Chemical synthesis and magnetic properties of nanocrystalline $FeMoN_2$, *J. Cryst. Growth* 191(1–2), 92 (1998)
45. A. Togo and I. Tanaka, First principles phonon calculations in materials science, *Scr. Mater.* 108, 1 (2015)
46. F. Mouhat and F. M. C. X. Coudert, Necessary and sufficient elastic stability conditions in various crystal systems, *Phys. Rev. B* 90(22), 224104 (2014)
47. X. Li, X. Wu, and J. Yang, Half-metallicity in $MnPSe_3$ exfoliated nanosheet with carrier doping, *J. Am. Chem. Soc.* 136(31), 11065 (2014)
48. C. C. Tho, X. Feng, L. Cao, G. Wang, S. J. Liang, C. S. Lau, S. D. Guo, and Y. S. Ang, Ultrathick $MA_2N_4(M'N)$ intercalated monolayers with sublayer-protected Fermi surface conduction states: Interconnect and metal contact applications, *Adv. Phys. Res.* 2300156, 2300156 (2024)
49. J. B. Goodenough, Theory of the role of covalence in the perovskite-type manganites $[La,m(II)]MnO_3$, *Phys. Rev.* 100(2), 564 (1955)
50. Y. Wang, X. Xu, W. Ji, S. Li, Y. Li, and X. Zhao, Exploitable magnetic anisotropy and half-metallicity controls in multiferroic van der Waals heterostructure, *npj Comput. Mater.* 9(1), 223 (2023)
51. C. Liu, G. Zhao, T. Hu, Y. Chen, S. Cao, L. Bellaiche, and W. Ren, Ferromagnetism, Jahn–Teller effect, and orbital order in the two-dimensional monolayer perovskite Rb_2CuCl_4, *Phys. Rev. B* 104, L241105 (2021)
52. M. R. K. Akanda and R. K. Lake, Magnetic properties of $NbSi_2N_4$, VSi_2N_4, and VSi_2P_4 monolayers, *Appl. Phys. Lett.* 119(5), 052402 (2021)
53. T. M. Henderson, J. Paier, and G. E. Scuseria, Accurate treatment of solids with the HSE screened hybrid, *Phys. Status Solidi B* 248(4), 767 (2011)
54. J. Li, X. Li, and J. Yang, A review of bipolar magnetic semiconductors from theoretical aspects, *Fund. Res.* 2(4), 511 (2022)
55. T. A. Manz and N. G. Limas, Introducing ddec6 atomic population analysis. Part 1. Charge partitioning theory and methodology, *RSC Adv.* 6(53), 47771 (2016)
56. A. S. Botana and M. R. Norman, Electronic structure and magnetism of transition metal dihalides: Bulk to monolayer, *Phys. Rev. Mater.* 3(4), 044001 (2019)
57. T. Barnowsky, S. Curtarolo, A. V. Krasheninnikov, T. Heine, and R. Friedrich, Magnetic state control of non-van der Waals 2D materials by hydrogenation, *Nano Lett.* 24(13), 3874 (2024)
58. K. Wang, K. Ren, Y. Hou, Y. Cheng, and G. Zhang, Physical insights into enhancing magnetic stability of 2D magnets, *J. Appl. Phys.* 133(11), 110902 (2023)
59. Y. Wang and Y. Ding, Tunable structural phases and electronic properties of group V MSi_2N_4 (M = V, Nb, Ta) nanosheets via surface hydrogenation: A first-principles study, *J. Mater. Chem. C* 11(48), 17034 (2023)
60. Y. Wu, L. Deng, J. Tong, X. Yin, F. Tian, G. Qin, and X. Zhang, Ferrovalley and topological phase transition behavior in monolayer $Ru(OH)_2$, *J. Mater. Chem. C* 11(40), 13714 (2023)
61. X. Zhang, Q. Lu, W. Liu, W. Niu, J. Sun, J. Cook, M. Vaninger, P. F. Miceli, D. J. Singh, S. W. Lian, T. R. Chang, X. He, J. Du, L. He, R. Zhang, G. Bian, and Y. Xu, Room-temperature intrinsic ferromagnetism in epitaxial $CrTe_2$ ultrathin films, *Nat. Commun.* 12(1), 2492 (2021)
62. H. R. Fuh, C. R. Chang, Y. K. Wang, R. F. L. Evans, R. W. Chantrell, and H. T. Jeng, New type single-layer magnetic semiconductor in transition-metal dichalcogenides VX_2 (X = S, Se and Te), *Sci. Rep.* 6(1), 32625 (2016)
63. B. Huang, G. Clark, E. Navarro-Moratalla, D. R. Klein, R. Cheng, K. L. Seyler, D. Zhong, E. Schmidgall, M. A. McGuire, D. H. Cobden, W. Yao, D. Xiao, P. Jarillo-Herrero, and X. Xu, Layer-dependent ferromagnetism in a van der Waals crystal down to the monolayer limit, *Nature* 546(7657), 270 (2017)
64. C. Gong, L. Li, Z. Li, H. Ji, A. Stern, Y. Xia, T. Cao, W. Bao, C. Wang, Y. Wang, Z. Q. Qiu, R. J. Cava, S. G. Louie, J. Xia, and X. Zhang, Discovery of intrinsic ferromagnetism in two-dimensional van der Waals crystals, *Nature* 546(7657), 265 (2017)
65. Y. Deng, Y. Yu, Y. Song, J. Zhang, N. Z. Wang, Z. Sun, Y. Yi, Y. Z. Wu, S. Wu, J. Zhu, J. Wang, X. H. Chen, and Y. Zhang, Gate-tunable room-temperature ferromagnetism in two-dimensional Fe_3GeTe_2, *Nature* 563(7729), 94 (2018)
66. J. Gong, G. Ding, C. Xie, W. Wang, Y. Liu, G. Zhang, and X. Wang, Genuine Dirac half-metals in two-dimensions, *Adv. Sci.* 11, 2307297 (2024)
67. X. Wang, X. P. Li, J. Li, C. Xie, J. Wang, H. Yuan, W. Wang, Z. Cheng, Z. M. Yu, and G. Zhang, Magnetic second-order topological insulator: An experimentally feasible 2D $CrSiTe_3$, *Adv. Funct. Mater.* 33(49), 2304499 (2023)
68. Y. Yao, L. Kleinman, A. H. MacDonald, J. Sinova, T.

Jungwirth, D. S. Wang, E. Wang, and Q. Niu, First principles calculation of anomalous Hall conductivity in ferromagnetic bcc Fe, *Phys. Rev. Lett.* 92(3), 037204 (2004)

69. Y. Yao and Z. Fang, Sign changes of intrinsic spin Hall effect in semiconductors and simple metals: First-principles calculations, *Phys. Rev. Lett.* 95(15), 156601 (2005)
70. S. J. Zhang, C. W. Zhang, S. F. Zhang, W. X. Ji, P. Li, P. J. Wang, S. S. Li, and S. S. Yan, Intrinsic Dirac half-metal and quantum anomalous Hall phase in a hexagonal metal-oxide lattice, *Phys. Rev. B* 96(20), 205433 (2017)
71. X. Zhu, Y. Chen, Z. Liu, Y. Han, and Z. Qiao, Valley-polarized quantum anomalous Hall effect in van der Waals heterostructures based on monolayer jacutingaite family materials, *Front. Phys.* 18(2), 23302 (2023)
72. X. Kong, L. Li, L. Liang, F. M. Peeters, and X. J. Liu, The magnetic, electronic, and light-induced topological properties in two-dimensional hexagonal FeX_2 (X = Cl, Br, I) monolayers, *Appl. Phys. Lett.* 116(19), 192404 (2020)
73. H. Sun, S. S. Li, W. X. Ji, and C. W. Zhang, Valley-dependent topological phase transition and quantum anomalous valley Hall effect in single-layer RuClBr, *Phys. Rev. B* 105(19), 195112 (2022)
74. Q. F. Liang, R. Yu, J. Zhou, and X. Hu, Topological states of non-Dirac electrons on a triangular lattice, *Phys. Rev. B* 93(3), 035135 (2016)
75. C. Si, K. H. Jin, J. Zhou, Z. Sun, and F. Liu, Large-gap quantum spin Hall state in MXenes: d-band topological order in a triangular lattice, *Nano Lett.* 16(10), 6584 (2016)
76. Z. Zhang, L. Zhao, and J. Shi, Mechanics and strategies for wrinkling suppression: A review, *Front. Mech. Eng.* 8, 910415 (2022)
77. S. Yang, Y. Chen, and C. Jiang, Strain engineering of two-dimensional materials: Methods, properties, and applications, *InfoMat* 3(4), 397 (2021)
78. J. Wang, L. He, Y. Zhang, H. Nong, S. Li, Q. Wu, J. Tan, and B. Liu, Locally strained 2D materials: Preparation, properties, and applications, *Adv. Mater.* 36(23), 2314145 (2024)